A study of picosecond laser–solid interactions up to 10^{19} W cm^{-2}

F. N. Beg, A. R. Bell, A. E. Dangor, C. N. Danson,[a] A. P. Fews,[b] M. E. Glinsky,[c]
B. A. Hammel,[c] P. Lee, P. A. Norreys,[a),d] and M. Tatarakis
Imperial College of Science, Technology & Medicine, Prince Consort Road, London, SW7 2AZ, United Kingdom

(Received 16 August 1996; accepted 2 October 1996)

The interaction of a 1053 nm picosecond laser pulse with a solid target has been studied for focused intensities of up to 10^{19} W cm^{-2}. The maximum ion energy cutoff E_{max} (which is related to the hot electron temperature) is in the range 1.0–12.0 MeV and is shown to scale as $E_{max} \approx I^{1/3}$. The hot electron temperatures were in the range 70–400 keV for intensities up to 5×10^{18} W cm^{-2} with an indication of a high absorption of laser energy. Measurements of x-ray/γ-ray bremsstrahlung emission suggest the existence of at least two electron temperatures. Collimation of the plasma flow has been observed by optical probing techniques. © *1997 American Institute of Physics.* [S1070-664X(97)01701-1]

I. INTRODUCTION

The development of the technique of chirped pulse amplification (CPA)[1] has enabled high power lasers to produce multiterrawatt femtosecond and picosecond laser pulses which can be focused on target at intensities that were previously inaccessible in the laboratory. Many interesting new physical phenomena have been predicted in this new regime. For instance, the laser pulse is predicted to bore a hole in the plasma due to the radiation pressure which reaches 3.0 Gbar at intensities of 1×10^{19} W cm^{-2}.[2] Exceedingly large magnetic fields are expected to develop during the interaction and affect both lateral energy transport during the interaction and the overall plasma expansion.[3] Some interesting new applications have been proposed for these ultrahigh intensity pulses—such as the development of a MW coherent soft x-ray source from harmonics generated by the relativistic current associated with electrons driven back and forth across the vacuum—solid interface[4,5] and in the fast ignitor scheme for inertial confinement fusion (ICF).[6]

The processes of energy absorption in the presence of very steep density gradients is a topic of lively debate at the present time. At high intensities, a number of collisionless processes become important. These include resonance absorption,[7] vacuum heating,[8,9] skin-layer heating,[10,11] and, at normal incidence, $\mathbf{v}\times\mathbf{B}$ heating.[2,12] In the absence of ultrafast diagnostics, time integrated measurements of the absorption, energy transference to ions and electrons, and their characteristic temperatures can help to clarify the applicability of the different models.

In earlier experiments with CO_2 ($\lambda=10.6$ μm) and Nd-glass ($\lambda=1.064$ μm) lasers, pulses ranged from tens of picoseconds to nanoseconds duration, and values of $I\lambda^2$ up to 3×10^{18} W cm^{-2} μm^2 were obtained. Significant ponderomotive steepening of the plasma density profile around the critical density surface was observed. The electron temperature scaling with $I\lambda^2$ was examined experimentally at a large number of laboratories around the world, and a picture of the electron temperature being mainly determined by resonance absorption emerged (for a review see Gitomer *et al.*[13] and all references therein).

For (sub)-picosecond laser pulses that are incident onto solid targets, electron temperature measurements have been made at a number of laboratories.[14–21] A recent compilation has shown that these scale as $T_{hot} \sim (I\lambda^2)^{1/3-1/2}$ and are consistent with particle in cell (PIC) calculations.[22] At the highest available intensities at present ($I=10^{19}$ W cm^{-2}) and an intensity contrast ratio of $1:10^{-8}$, Malka and Miquel[23] have shown that the electron temperature is dominated by the ponderomotive potential for those electrons directed along the axis of the laser beam and temperatures of 1 MeV have been measured.

In this paper, a series of experiments that were conducted on the CPA beam line of the Nd:glass laser VULCAN[24] are reported for laser–plasma interactions with solid targets for intensities between 1×10^{17} and 10^{19} W cm^{-2}. In this case, the intensity contrast ratio was $1:10^{-6}$. It is shown for the first time that the maximum ion energy (which is directly related to the hot electron temperature) associated with the fast electron driven plasma expansion scales as $E_{max}=1.2(\pm0.3)\times10^{-2}\ I^{0.313\pm0.03}$ keV (where I is in W cm^{-2}). Measurements of the x-ray/γ-ray bremsstrahlung emission are indicative of the existence of at least two electron temperatures. The electron and ion measurements are consistent with an extrapolation of the nanosecond high intensity laser–plasma interactions made with CO_2 lasers to these higher values of $I\lambda^2$. Collimation of the plasma flow has been observed by schlieren, shadowgraphic, and interferometric techniques. The various absorption processes are assessed in the light of these measurements and similar results reported in the literature.

II. EXPERIMENTAL CONFIGURATION AND PLASMA DIAGNOSTICS

A. The laser system and target chamber

The experiments were conducted using the CPA beamline of the VULCAN Nd:glass laser.[24,25] This laser delivered

[a)]Permanent address: Central Laser Facility, Rutherford Appleton Laboratory, Chilton, Didcot, Oxon OX11 0QX, United Kingdom.
[b)]Permanent address: H. H. Wills Physics Laboratory, University of Bristol, Royal Fort, Tyndall Ave., Bristol BS8 1TL, United Kingdom.
[c)]Permanent address: Lawrence Livermore National Laboratory, Livermore, California 94550.
[d)]Electronic mail: p.norreys@rl.ac.uk

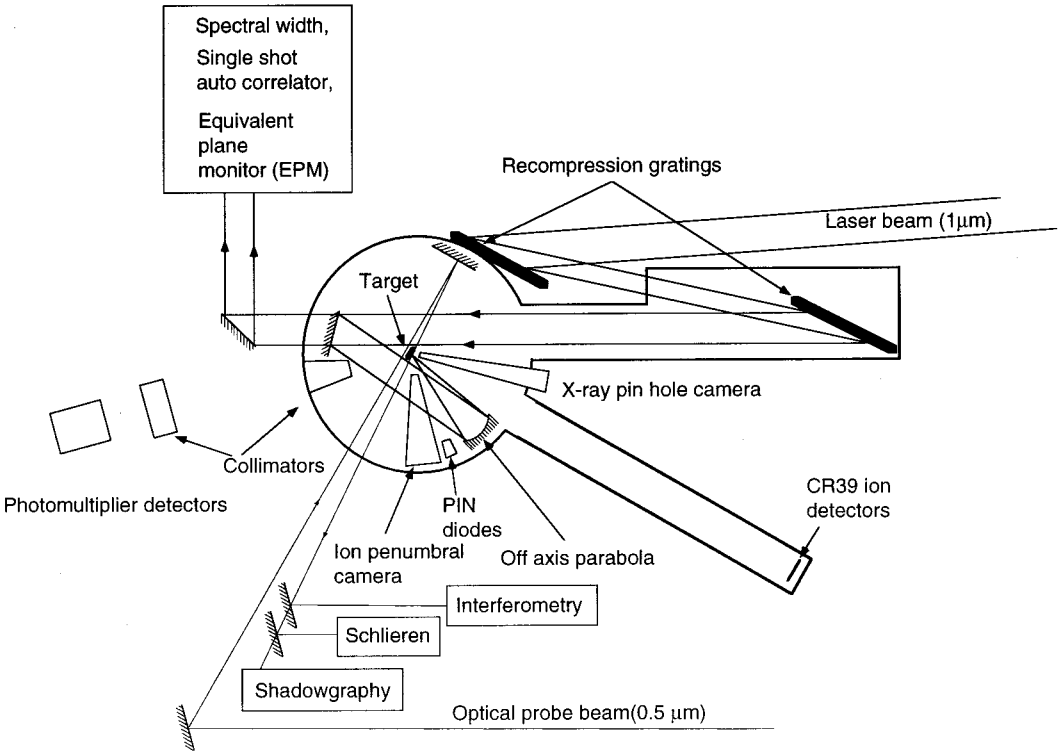

FIG. 1. Experimental setup of the VULCAN CPA target chamber.

laser pulses on target of up to 30 J. An additively mode-locked Nd:LMA short pulse oscillator provided pulse lengths ranging from 700 fs to 1.3 ps at a wavelength of 1054 nm and bandwidth of 2.6 nm. Similarly, an additively mode-locked Nd:YLF oscillator provided pulses of 2.5–4 ps at a wavelength of 1053 nm and bandwidth of 0.6 nm. These pulses were stretched to 200 and 80 ps for the Nd:LMA and Nd:YLF oscillators, respectively. They were then amplified in the laser chain and recompressed using large area diffraction gratings. A 95% turning mirror located after the recompression gratings steered the beam onto an $f/4.2$ 44 cm off axis parabolic mirror which focused the radiation onto target, as shown in Fig. 1. The turning mirror allowed 5% transmission of the laser energy for measurements of the laser spectrum, the pulse duration by a single shot autocorrelator and the focal spot quality by an equivalent plane monitor. The contrast ratio was measured by a third order autocorrelator to be 10^{-6} for both oscillators.

The p-polarized laser energy was focused onto target at an angle of 30° to the target normal. Figure 1 shows a schematic outline of the target chamber and the positions in the horizontal plane of the principal plasma diagnostics that were employed. Various target materials were irradiated, and will be detailed in the following sections that describe the diagnostic equipment and techniques used in the experiments.

B. X-ray and ion imaging diagnostics

High-resolution imaging techniques are required in order to accurately determine the focal spot size. Conventional x-ray pinhole imaging has a resolution that is limited both by the size of the pinhole that can be manufactured and by diffraction effects which are proportional to the x-ray wavelength being imaged (~ 5 μm at 2.5 keV). Hence the proven technique of maximum entropy penumbral imaging was used to provide the required high-resolution (~ 2 μm) images of both the energetic ions and x rays.[26] The technique has previously been employed to measure the shape of implosion cores of ICF targets in three dimensions from alpha particle emission. A charge coupled device (CCD) x-ray penumbral imaging camera was formed using a gold aperture of 80 μm diameter located 12 mm from the target with a magnification of 10. Al filters of 5 μm and 25 μm were used to image low and high energy shots, respectively. A similar aperture was used in the ion penumbral imaging camera. In this case, the CR-39 detector had dimensions of 50 mm$\times$50 mm and the magnification ranged from 3 to 10 in the different experiments. X-ray pinhole cameras with ~ 10 μm resolution were used to provide comparative information about the gross structure around the focal spot region.

C. Focal spot size determination

To ensure that the spot size was minimized and the intensity on target was maximized, massive glass slab targets that had been overcoated with 200 nm thick, 10 μm wide Al alignment cross wires were irradiated with 50 mJ shots from the VULCAN laser and the size of x-ray emission was measured by the x-ray penumbral imaging camera. The target was then moved in the vertical plane, and a full energy shot delivered to the clean target surface. Figure 2 shows the x-ray emission spot size in the horizontal and the vertical planes for the low energy shots. It can be seen that the best spot size was 9 μm full width at half maximum (FWHM) in

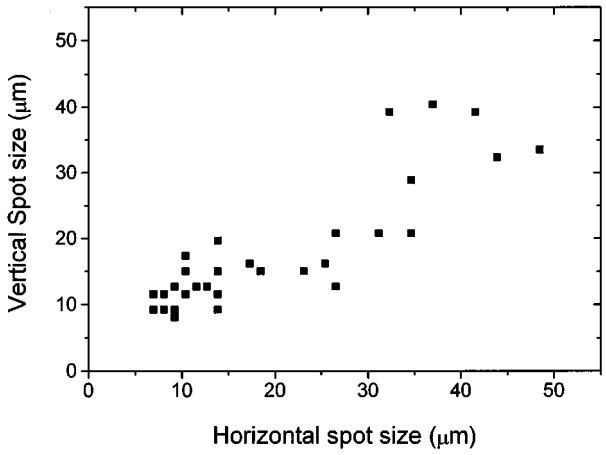

FIG. 2. Vertical against horizontal spot size determination by x-ray penumbral imaging.

both planes, with an average spot size of ~12 μm. The difference in focusing between a full energy shot and the lower energy 50 mJ shots was not affected by the total B-integral (B) in the laser chain which was calculated to be no more than $B=0.8$ at 1 ps for 24.0 J on target.

A detailed characterization experiment of the focusability of the VULCAN CPA beam has been performed using a long (3 m) focal length off axis parabola, minimizing pinhole closure of full energy shots.[25] Energy through pinhole measurements established that the beam was ~3.5 times diffraction limited, i.e., that 50% of the energy was contained within a 16 μm focal spot for the 0.44 m focal length off-axis parabola. It has been the experience of the present authors that the focusability of the VULCAN beam has varied with different experiments, and that the focal spot quality requires regular assessment during experimental campaigns. The fact that the focal spot quality can be better than in the characterization experiment has been independently corroborated by spatial coherence measurements of the fourth harmonic which have shown the effective source size to be between 10 and 12 μm,[27] which are similar to the results in Fig. 2.

D. CR-39 plastic nuclear track detectors

The energetic ion emission was recorded by CR-39 plastic nuclear track detectors.[28] CR-39 records charged nuclear particles as tracks which are etched into the surface of the detector after exposure. A separate etch track is produced by each incident ion and the dimensions and depth of penetration of the track enables the energy and atomic number of the ions to be uniquely determined. CR-39 detectors are sensitive to ions with energies $\geqslant$100 keV/nucleon. The detectors were covered in an array of up to 12 Mylar filters which increased in thickness by 2.5 μm and eight steps of Al of thickness 25 μm. Each step is sensitive to a different energy interval, giving an energy resolution of 0.1 MeV in the range 0.1–6.0 MeV. In addition, a aluminum wedge of thickness 0.2 mm at one end and 1.1 mm at the other was used to measure ions with energies up to 14.0 MeV. In all shots, one piece of CR-39 was placed in the normal incidence direction, either on the chamber wall at a distance of 55 cm or at the end of an extension tube 2.5 m from the chamber center.

TABLE I. X-ray filters for pin diodes detectors.

Filter pair	Peak energy (keV)	Energy window (keV)
10 μm Cu+20 μm Al and 40 μm Ti+20 μm Al	8	6–9
250 μm Al and 2 mm Al	14	9–20
2 mm Al and 250 μm Cu+1 mm Al	22	18–34
250 μm Cu+1 mm Al and 1 mm Cu^+ 1 mm Al	42	28–60
250 μm Ta+100 μm Al and 1 mm Ta+100 μm Al	67	55–250

E. X-ray and γ-ray bremsstrahlung detectors

The detection of the x-ray bremsstrahlung radiation from the target was undertaken using an array of filtered pin diodes together with a pair of photomultiplier/scintillator detectors. To eliminate bremsstrahlung radiation emanating from energetic electrons and ions impinging on the wall of the chamber, collimating apertures were placed 20 cm from the target position inside the vacuum chamber. These consisted of 1.0 cm holes drilled through 20 cm of lead at an angle of 4° from the axis. Two photomultipliers (XP 2008) detectors, located 3.0 m from the target, were encased in 10 cm thick lead blocks with four 1.0 cm holes (also at 4° from the axis) which were aligned with the collimating apertures in the vacuum vessel. The photomultiplier detectors were filtered with 2–5 mm of lead. To eliminate fluorescence from γ-ray traversing the lead filters, 1.0 cm thick Al blocks were placed behind the filters. The scintillators consisted of NaI(Tl) crystals of diameter and length 2.54 and 5 cm, respectively. The detectors were calibrated with a 1.25 MeV ^{60}Co and a 665 keV ^{137}Cs source.

An array of eight Quantrad pin diodes with a 100 mm^2 active area biased at -300 V were also used. These were placed at 40 cm from the target. The active layer varied in thickness from 125 to 500 μm to increase the sensitivity of the detectors to the higher energy x-ray windows. The response time of the diodes was limited by the capacitance and the mobility of the charge carriers to the ns time scale so that the signals could be observed on an oscilloscope. The calibration of each detector was obtained from the manufacturer's data sheets. These were checked by comparison to the work of Corallo, Creek, and Murray.[29] The filters were chosen to define the energy windows, as detailed in Table I.

F. CCD detector for dispersionless x-ray K_α spectroscopy

The characteristic temperature of the energetic electrons that were generated in the interaction can be characterized by measuring the K_α x-ray emission that the energetic electrons induce when they pass through multilayer targets.[30–35] Measurement of the relative K_α x-ray fluorescent emission from two or more layers can yield an estimate of the number and energy of the electrons, taking into account (a) electron en-

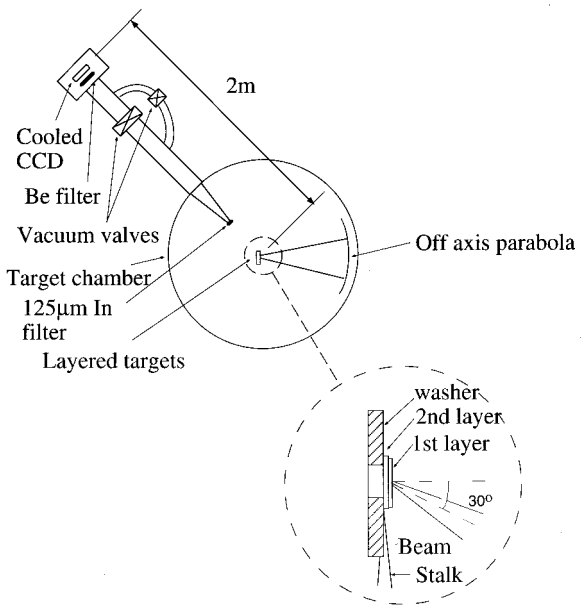

FIG. 3. Arrangement of K_α instrumentation.

ergy loss in the materials, (b) K shell ionization cross sections, (c) the number of K_α photons produced by an electron of a particular energy, (d) the x-ray mass absorption coefficients of the materials in the target.

Figure 3 shows a schematic layout of the technique. The targets consisted of: 25 μm Pd on 72 μm Sn; 47 μm Pd on 72 μm Sn; 25 μm Mo on 25 μm Sn; and 12 μm Mo on 25 μm Sn. The laser irradiated the Pd or Mo side of the metallic sandwich targets. These medium Z materials were chosen so that the number and energy of the photons detected from each layer lay within the dynamic range of the instrument, and the K shell binding energies were high enough to minimize K_α fluorescence induced from the plasma x-ray emission but were not above the usable range of the detector. The metallic layers were mounted on 5 mm diameter washers to prevent energetic electrons being guided around the back of the target by the self-generated magnetic field.

A 16-bit x-ray CCD (Reticon RA1024J with 10^6 13.5 μm$\times$13.5 μm pixels with a 4.5 μm thick depletion layer) was used for obtaining the x-ray spectra. The CCD was used in a single hit mode, i.e., where the collection efficiency of the CCD is chosen such that the probability that two photons interacting with one pixel is small. In this mode the value V_p read out from each pixel is directly proportional to the energy of the x-ray photon E_p. After the CCD is exposed, an image, composed of multiple single hits, is captured and stored on a computer. A histogram is then constructed of the number of hits against V_p and, to a first approximation, this histogram gives the x-ray spectrum. In this experiment, an ''isolated event'' histogram, i.e., a histogram consisting of only those pixels which contain more than 98% of the energy in a square containing 9 pixels, was used to construct the x-ray spectrum, as this greatly increased the signal to noise ratio compared with plain and ''summed event'' (the spread charge in the surrounding eight pixels of a centered event is added to the parent pixel) histograms.

The response function of the detector is the probability that a photon interacts with a pixel and this can be obtained from the mass absorption coefficients of silicon with the thickness of the dead and the depletion layers in the CCD chip together with the transmission of the 125 μm thick In filter. The detector was calibrated using a 4.1 mCi ^{109}Cd source for a 180 s exposure. This source decays to ^{109}Ag by electron capture and the silver emits K shell radiation in the ratio 83.4% at 22 keV and 16.4% at 25 keV. The detector energy response function was found to be linear with $E_p=0.0818(v_p-3.01)$ keV for photon energies between 17.5 keV$<E_p<$28.5 keV.

The resolution of the spectrometer is given theoretically by[36]

$$\delta E = 2.355\times E_0\left(N^2+\frac{0.11E}{E_0}\right)^{1/2}, \tag{1}$$

where δE is the energy resolution at full width at half maximum (FWHM) in eV, $E_0=3.7$ eV is the average energy required to produce an electron hole pair, and N is the root-mean-square readout noise of the CCD obtained by acquiring a ''dark'' image (an image taken without x rays and then processed in the same way as the data shots). From a dark image with $N=52$, the resolution was found to be 0.5 keV at 25 keV, compared to a minimum without dark noise of 0.2 keV. This agrees with the observed linewidths of $\sim$0.5 keV at 20–25 keV which are much greater than the actual linewidths ($\sim$0.5 eV). Such a resolution means that the lines from most ionization stages are indistinguishable.

Figure 4 shows an example of the K_α x-ray spectrum obtained when 8 J of energy in 2.5 ps was incident onto a metallic ''sandwich'' target consisting of 25 μm of Pd on 75 μm of Sn. To obtain an estimate of the number and energy of the electrons by K_α spectroscopy, K shell ionization cross sections[37] given by

$$\sigma_k = 7.92\times 10^{-14}\,\frac{\ln(U_k)}{E_k^2 U_k}\ \text{cm}^2 \tag{2}$$

(U_k is the ratio of the electron energy E to the K shell binding energy E_k) which used Spencer's fast electron energy deposition model for electron traversing cold material, x-ray mass absorption coefficients[38] and Krause's data on the number of K_α photons produced for a given electron energy were employed.[39] The targets were modeled as a series of thin planar targets. An electron at energy E_0 is propagated through the targets and the total K_α emission is calculated for the detector placed at an angle 35° to the target normal.

G. Schlieren, shadowgraphy, and interferometry layouts

The development of many MG magnetic fields are expected to develop during the interaction due to the very large density and temperature gradients ($\partial\mathbf{B}/\partial t\approx\nabla n\times\nabla T$) that are generated.[2,40,41] The magnetic field has been calculated to affect the overall plasma expansion profile.[42] Consequently, measurements of the plasma density profile after the interaction is of interest.

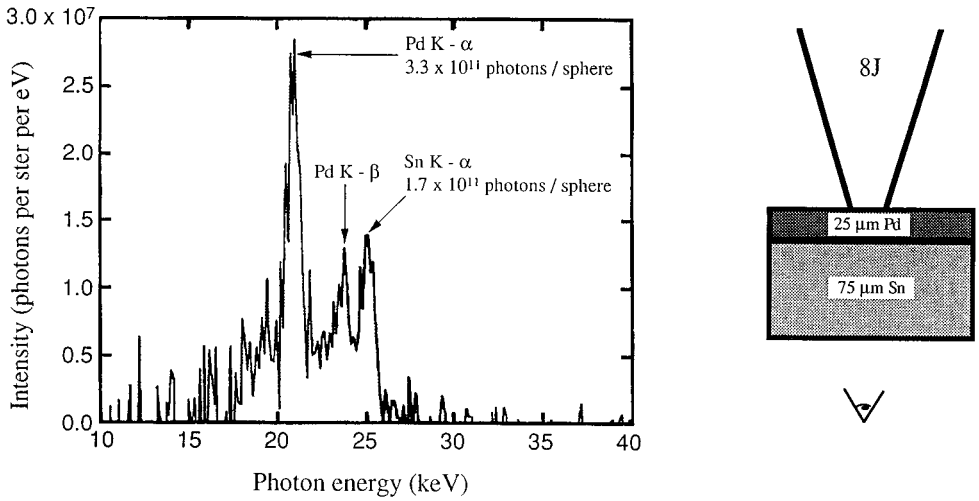

FIG. 4. Example of K_α x-ray emission obtained when an 8 J/2.5 ps pulse was incident onto a 25 μm Pd/75 μm Sn sandwich target.

Figure 1 shows the chamber layout for the optical diagnostics. A 1 ps, 10 mJ pulse was frequency doubled and timed to arrive at the chamber center at the same time as the main heating pulse. The optical probe beam was incident parallel to the target surface, i.e., at 90° to the target normal. Three channels were used for the optical probe beam: schlieren, shadowgraphy, and interferometry. All images were captured on CCD detectors. The schlieren and shadowgraphy optical elements are shown schematically in Fig. 5. A circular stop size of 0.27 mm diameter was employed in the schlieren photography.

Traditionally interferometry, involving a devided beam path, requires an extremely stable environment, high quality optical components and ultraprecise alignment to give useable output with ~1 ps pulse duration. To overcome this problem, a self-referencing cyclic shear interferometer was employed.[43] Fringes are produced by the interference of beams which propagate clockwise and anticlockwise around the path ABC in Fig. 6. The beam that follows the path ACB is expanded by the telescope, while the ABC beam is condensed. Interference takes place between the whole spatial extent of the ABC beam and a small fraction of the ACB beam. The interfering portion of the ACB beam can be considered as a reference beam, which has an effective phase front having phase gradients M^2 where M is the magnification of the telescope. If M is sufficiently large, then the reference beam can be considered to be a plane wave in comparison with the ABC beam.

For optimum fringe contrast, the two beams need to be of equal intensity and this is achieved by choosing a suitable reflectivity for the beam splitter. The telescope introduces an intensity ratio of M^2 between the two interfering beams. For $M=4$, the optimum reflectivity of the beam splitter is 6.25%. In practice, an uncoated wedged flat at 45° incidence has been found to give satisfactory performance and was used in this experiment.

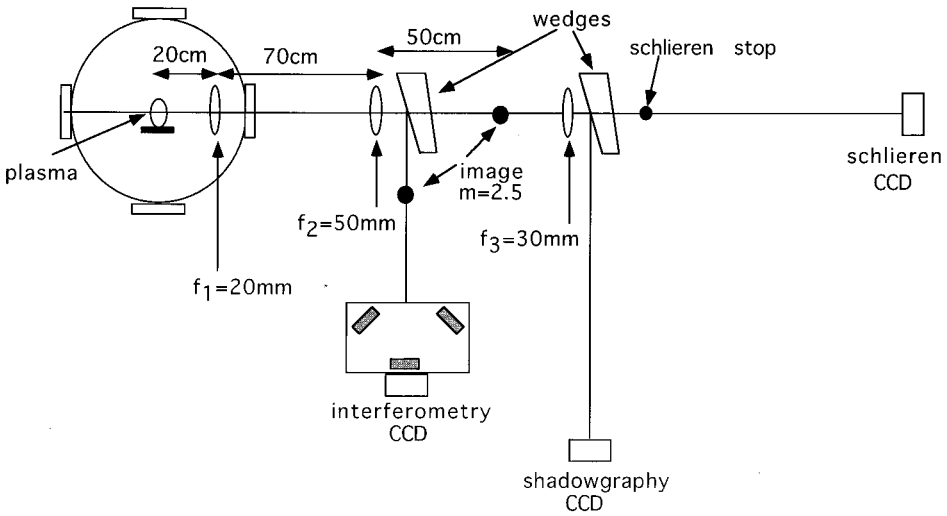

FIG. 5. Optical arrangement for shadowgraphy, schlieren, and interferometry.

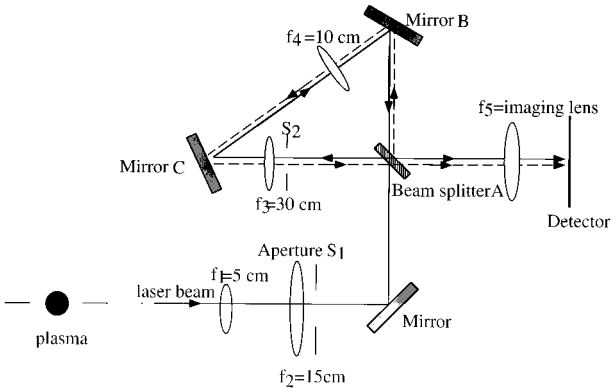

FIG. 6. Optical layout of the interferometer.

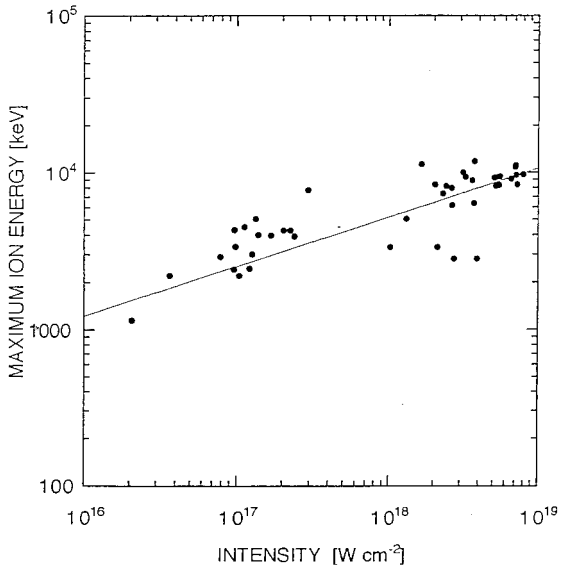

FIG. 7. Maximum ion energies recorded in CR-39 detectors plotted against incident intensity.

III. RESULTS

A. Ion velocity and electron temperature measurements

The targets in this series of experiments ranged from CH overcoated glass slabs to Cu and CH disk targets (which were 270 or 550 μm in diameter, and 13 or 36 μm in thickness). In all cases, the energetic ion emission associated with the fast electron driven plasma expansion that were measured in the CR-39 plastic nuclear track detectors were predominantly from protons. These originate from a thin CH contamination of the target surface. No differences in the ion emission was observed between the different targets materials which were irradiated. The ion spectra in most of the shots show an exponential decreasing profile with increasing ion energy, followed by a sharp cutoff.[44] This cutoff and surface contamination was first observed by Pearlman and Morse[45] who attributed the cutoff to charge separation. This limits the ion velocities by forming a non-neutral electrostatic sheath which truncates the exponential density profile. Figure 7 shows the maximum ion energy recorded in the CR-39 detectors plotted against incident irradiance. A least-square fit to the data gives.

$$E_{\max}=1.2\pm(0.3)\times10^{-2}[I/(\mathrm{W\,cm^{-2}})]^{0.313\pm0.03}\ \ \mathrm{keV}. \tag{3}$$

In an isothermal rarefaction model, first proposed by Tan, McCall, and Williams,[46] the self-similar solution for a single ion species planar expansion has the form $n=n_0e^{-v/c}$ (where n is the density for those ions traveling at velocity v, n_0 is the density at the emitting surface and c is the ion sound speed). The effect of introducing charge separation is to introduce a maximum ion velocity $V_{\max}$ when the plasma scale length equals the Debye length λ_D: $ct=\lambda_D$. Substituting the last expression into the first and solving for $V_{\max}$ gives: $V_{\max}=c\,\ln(n_0/n)=2c\,\ln(\omega_{pi}t)$ (where n is the density at which the $ct=\lambda_D$ equality is satisfied and ω_{pi} is the ion plasma frequency). Provided that the logarithmic expression is slowly varying, then the hot electron temperature is proportional to $V_{\max}^2$ and therefore $E_{\max}$.

Tan and colleagues showed that the measured maximum ion velocity is proportional to the laser intensity on target and to the hot electron temperature, at least for longer pulse duration interactions in the range 10^{14}–3×10^{18} W cm^{-2} μm^2. Indeed, *the maximum ion energies measured under our conditions follow exactly the same scaling with intensity as those shown by Tan and colleagues*. A similar relationship between T_{hot} and $E_{\max}$ has been confirmed in the much more detailed theoretical model of Kishimoto, Mima, and colleagues.[47]

To determine the electron temperature by K_α x-ray spectroscopy, calculations of the ratio of the number of the K_α photons from the first and second flourescent layers as a function of the electron temperature and detector response (as outlined in Sec. II F) are required. Figure 8 shows such a plot for electrons which have a Maxwellian distribution together with the experimentally determined ratios for the different sandwich target materials irradiated. The experimental points lie within the range 70–200 keV. Electron temperatures deduced from different electron velocity distributions are left to the discussion in Sec. IV.

Both the x-ray and ion penumbral imaging cameras had to be removed for these K_α target shots because their large diameter obstructed the instruments. The intensity on target was estimated by comparing measurements of the maximum ion energies for this data series with that established in Fig. 7. Figure 9 shows a plot of the electron temperature against incident laser energy. Taking the nominal spot size associated with $\times3.5$ diffraction limited operation of the VULCAN laser, the intensities on target were in the range 1.1×10^{18} –7.0×10^{18} W cm^{-2}. However, the maximum ion energies for all the metallic layer targets were, on average, lower than those presented in Fig. 7, which suggests that the intensities for these targets were in the range 1×10^{17} W cm^{-2} to 6×10^{17} W cm^{-2}.

There is an indication from Fig. 8 that the target materials irradiated may influence the deduced electron temperature, i.e., the desired temperatures are obtained by matching the electron penetration to the target layer thickness. How-

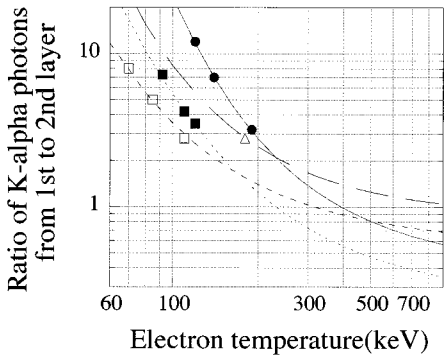

FIG. 8. Ratio of K_α photons from the first to second layer against electron temperature for various metallic layer targets: Solid circles (measured) and solid line (calculated) ratios for 47 μm Pd/72 μm Sn; open triangle and long chain for 25 μm Mo/25 μm Sn; solid squares and dotted line for 25 μm Pd/72 μm Sn; open squares and small chain 12 μm Mo/25 μm Sn.

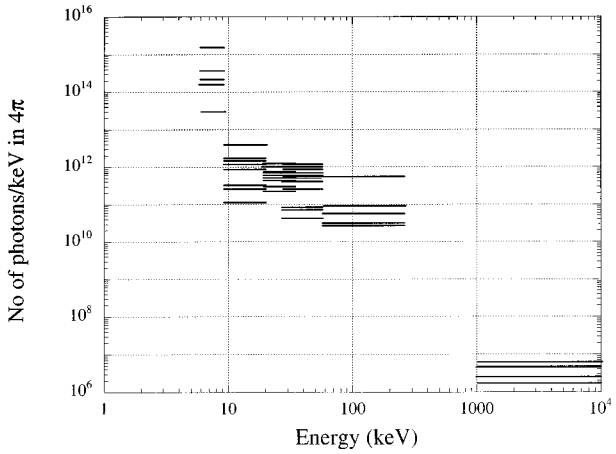

FIG. 10. X-ray spectrum indicating the existance of at least two electron temperatures for CD targets at average intensity 5×10^{18} W cm^{-2}.

ever when these temperatures are plotted against laser energy, as in Fig. 9, this trend does not appear to be significant.

Figure 10 shows a plot of the comparative x-ray bremsstrahlung emission measured in each of the pin-diodes and photomultipliers. The data were integrated over a number of shots (the intensity on target was $5.0(\pm3.0)\times10^{18}$ W cm^{-2} for plastic CD targets). It is interesting to note that it is not possible to assign a single temperature to the x-ray emission spectrum. Instead, the data suggests the presence of at least two electron temperatures. For instance, fitting a temperature through the first three lowest energy points in Fig. 10 indicates an electron temperatures in the range 1.0–3.0 keV. Similarly, a fit through the last three highest energy points is indicative of an electron temperature of 390 keV. However, some care is required in interpreting these electron temperatures due, in part, to the scatter in the measurements and, more importantly, to the limited spectral range of the detectors.

Figure 11 shows the number of 4 MeV photons plotted against incident intensity for a low Z (CH) materials. It is interesting to note that the number of 4 MeV photons increases by two orders of magnitude with a just factor of ~2 increase in intensity. This is probably due to the contribution to the bremsstrahlung emission from the high energy electrons at the tail end of the velocity distribution. This tail is, of course, very sensitive to both the electron temperature and to the exact form of the electron velocity distribution. Given this, it is interesting to note that the observed dramatic increase in the number of 4 MeV photons generated can be reproduced in calculations of the bremsstrahlung emission assuming a Maxwellian distribution, an electron temperature scaling of $T_{\rm hot}\sim(I\lambda^2)^{1/3}$, with an assumed hot electron temperature of 250 keV at 1×10^{18} W cm^{-2}.

At first there appears to be a discrepancy between K_α and the bremsstrahlung measurements, but the authors believe that this has been caused by the overestimate of the intensity on target for the K_α shots. Taking this into account, the hot electron temperatures derived from the K_α measurements, the γ-ray bremsstrahlung scaling with intensity and the integrated spectrum are all consistent with each other and with a temperature scaling of $T_{\rm hot}=100I^{1/3}$ keV (I is in 10^{17} W cm^2). This scaling is very similar to that measured with the HELIOS CO_2 laser at Los Alamos National Laboratory (see Fig. 5 of Gitomer *et al.*).[13]

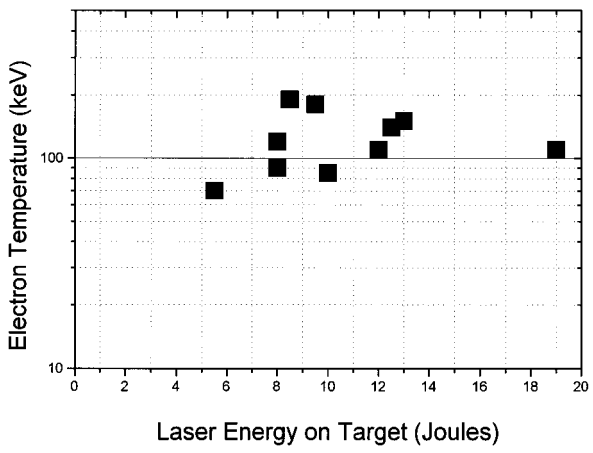

FIG. 9. Electron temperature (keV) against incident laser energy (Joules).

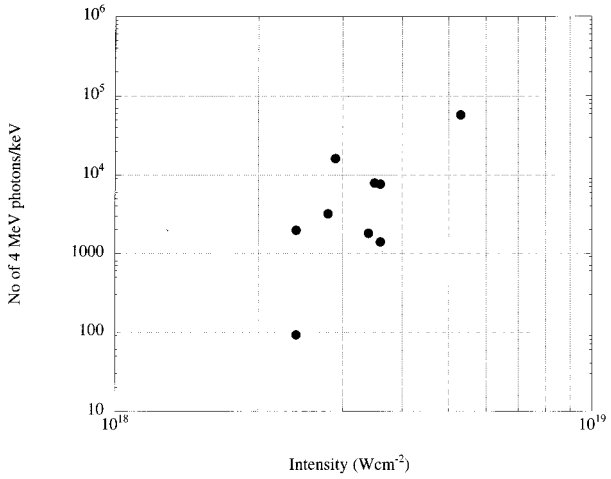

FIG. 11. Number of 4 MeV photons measured against incident intensity for CH targets.

The only discrepancy that arises is with the electron temperature that is derived from Tan *et al.* expansion model and these x-ray measurements.[46] They showed that the hot electron temperature scaled as $T_{\rm hot}=30\ I^{1/3}$ keV (I is again in units of 10^{17} W cm^2), i.e., lower by a factor of 3. However, as Tan *et al.* themselves point out, there is a large disparity (up to a factor of 5) between the temperatures derived from the expansion model and free electrons escaping from irradiated targets. This may be due to the limited applicability of a single ion species plasma expansion description. While it is clear that the existence of two hot electron temperatures cannot be ruled out from the integrated bremsstrahlung spectrum in Fig. 10 due to the limited spectral range, it is not clear that the difference between the x-ray and maximum ion energy methods of obtaining the electron temperature is physically significant.

The scaling of the hot electron temperature with intensity is, however, markedly different from those reported by Schnürer *et al.* who infer a hot electron temperature scaling of $T_{\rm hot}=I^{1.0-1.5}$ under similar conditions, albeit over a more limited intensity range.[16] The limited spectral resolution of the ionization chamber detector (their detector integrated all x-rays >50 keV) and the shielding that were employed (it is not clear that sufficient collimation was placed in the chamber to discriminate against energetic plasma impinging against the walls of the chamber) makes the interpretation of their bremsstrahlung signal much more difficult.

Nevertheless, these new measurements are consistent with an extrapolation to higher values of $I\lambda^2$ of the data taken with longer pulses. The measurements described in this section strongly suggest that the dominant absorption process is resonance absorption.

B. Optical probing

A number of interesting observations were made when a frequency doubled optical probe beam was used to measure the expansion profile of the plasma after the interaction pulse. Firstly, a significant amount of plasma light emission masked the probe signal in interferometric measurements. The main source of second harmonic emission is that generated by the relativistic current associated with electrons being dragged back and forth across the steepened density profile and that the harmonics are generated when the electron bunch up as the re-enter the overcritical plasma, i.e., they are localized near to the critical density surface.[4,5] To avoid this problem, the target was very slightly tilted to mask the self-generated second harmonic emission.

Figure 12 shows a representative (a) shadowgraphic and (b) schlieren image of the plasma profile 1.3 ns after the interaction pulse. For the schlieren, the minimum detectable density is $\sim 1.3\times10^{18}$ cm^{-3} for the stop size and focal length of the lens. The dark region across section AA' expands in the axial direction and across section BB' along the target surface. For low Z targets we deduce at early times (0–14 ps) an expansion velocity of 2.3×10^8 cm s^{-1} (29 keV/nucleon), at 260 ps a velocity of 4.5×10^7 cm s^{-1} and at later times (1.3 ns) a velocity of 2.4×10^7 cm s^{-1} (1 keV/nucleon). Extrapolating to $t=0$ shows that the initial radius is about 70 μm when the axial position is zero. This may have been

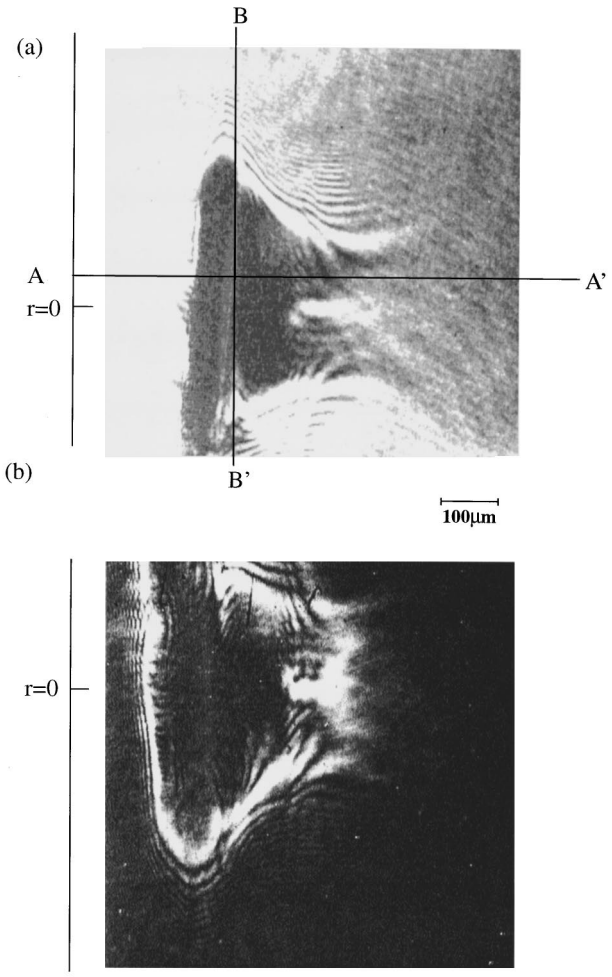

FIG. 12. Simultaneous (a) shadowgraphic (b) schlieren images of a CH target (diameter 550 μm and thickness 36 μm) irradiated at 2×10^{18} W cm^{-2} taken at a delay of at 1.3 ns with respect to the heating pulse.

caused either by the return current of the plasma or by the laser beam waste producing a plasma outside the focal region. It is also very interesting to note in both photographs that light appears at $r=0$ at the tip of the plasma surrounded by a dark region. This implies a high density gradient parallel to the target surface and the density appears to increase towards the edge of the plasma.

Figure 13 shows an interferogram taken at 400 ps after the main pulse on a 180 μm thick CD polystyrene target when 19.3 J was incident on target in a pulse length of 1.3 ps. The density profile generated through sections $Z1$ and $Z2$ at 83 and 100 μm from the target surface respectively are shown in Fig. 14 by Abel inversion of the fringe shift. These profiles clearly show a dip in the density in a cone defined by the laser spot size on the target. A divergence half angle of $\sim 16°$ can be deduced from the displacement of the density peaks in the two different positions.

It is interesting to note that a similar density profile was observed *during* the interaction pulse was observed by Attwood *et al.*[48] for a $I=3\times10^{14}$ W cm^{-2}/30 ps/1.06 μm laser pulse. The divergence angle derived from Fig. 14 are consistent with the results of the collimation of the plasma flow that were reported in earlier work.[42,44] This collimation was

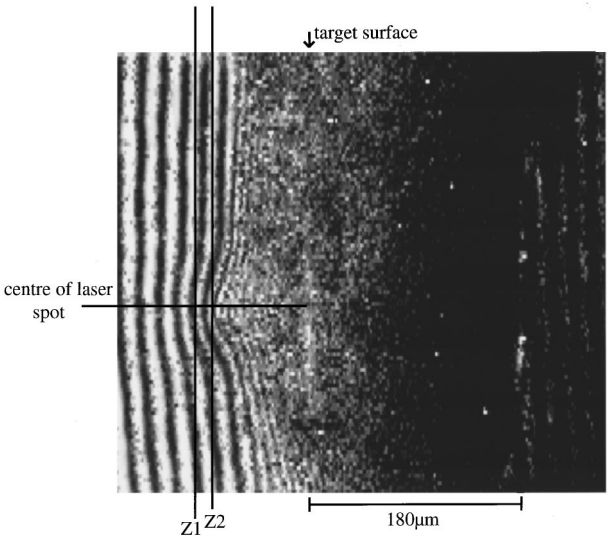

FIG. 13. Interferometric image taken at 400 ps after the peak of the heating pulse.

attributed to the possible generation of a multi-MG magnetic field that pinched the plasma flow onto the target normal [see Fig. 7(a) in Ref. 42].

IV. DISCUSSION

In this section, the limitations that must be considered in the K_a measurements are presented, an assessment is made of the measurements in the context of other published data and absorption processes and finally the cause of the two temperature phenomena is briefly discussed.

The greatest uncertainty in the determination of the fast electron temperature from measurement of the K_α x-ray spectra is that the electrons are traversing and depositing their energy through cold metallic materials. If Spitzer rather than metallic conductivity is assumed, then resistive inhibition in significantly increased and much larger electron temperatures (~600 keV) are required to penetrate through to the second Sn layer. Similarly, if the electrons are assumed to be monoenergetic rather than Maxwellian, then the energy

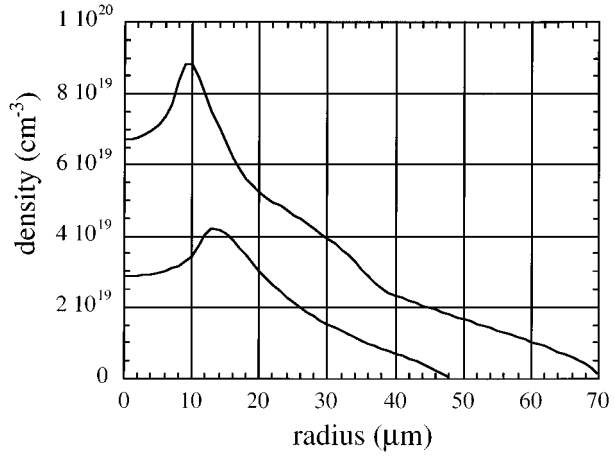

FIG. 14. Density profile deduced from Fig. 14 using Abel inversion.

of the electrons needs to be increased by a factor of 3 to account for the observed K alpha yield when traversing cold metallic layers. In the latter case, these higher electron energies lead to unphysical energy absorption fractions and can be discounted on this basis. Other possible sources of error are (a) the assumption that the electrons are effectively a planar source (b) the amount of backscattered electrons has been neglected in the calculations (c) electrons slow down continuously in the material. Furthermore, it is assumed that K_α fluorescence from the x-ray target plasma is negligible, which not unreasonable because the 3 keV measured electron temperature in the target plasma in Fig. 10 must be considered as a upper limit, as discussed in Sec. III A.

In the light of the assumptions used in the K_α measurement technique, errors can arise in assigning the number of electrons that generate the observed K_α emission. Initial calculations suggest that 40% of the laser energy is transferred to the energetic electrons that penetrate the target material, but this figure must be treated with some caution. For instance, Luther-Davies, Perry, and Nugent have reported measurements for 1064 nm, 20 ps, 3×10^{17} W cm^{-2} irradiation of K_α targets. Using the same data, they arrive at electron fractions that differ by a factor a 5 depending upon the assumptions used in the different electron transport models.[35] Given these constraints, confirmation of the high transference of laser energy into hot electrons deposited in the target must await a future experimental campaign.

To place all of these measurements in the context of general absorption processes, it is instructive take Gibbon's model based upon mobile ion boosted frame of reference particle-in-cell (PIC) calculations.[9] For oblique angles of incidence, ions are initially stationary and electrons are pulled out into the vacuum by a component of the electric field normal to the target. A time averaged $v\wedge B$ force acting away from the target surface is generated, producing a dc electric field that inhibits further electron exits from the plasma. At the same time the ponderomotive force pushes on the overdense plasma, generating a shock propagating into the plasma. The same dc electric field that keeps the electrons in the target ensures that ions are rapidly pulled out. As the ion expansion proceeds, the dc electric field is carried outwards into the shelf and the barrier that prevents efficient vacuum absorption is removed. The result is that a large proportion of the laser energy is absorbed via the vacuum or resonance absorption processes, depending on both the final density scale length and the time required to form the ion density shelf. Thus, a pulse with a temporal profile that is comparable to the ion shelf density formation time will result in a smaller absorption fraction than one that has a much longer duration. This may go some way to explain the differences in hot electron fractions reported between different laboratories operating at similar intensities but with differing pulse durations.[16,49] For normal incidence and s-polarized irradiation, the ion shelf forms much more slowly, if at all. This situation is similar to the fixed ion PIC simulations which result in much smaller absorption fractions[9] and may go some way to explain 10% absorption results reported by Price *et al.*[11]

In reality, the heating pulse has both an intensity ped-

estal associated with the residual dispersion and amplified spontaneous emission (ASE) in the laser chain. It also has a time-dependent pulse shape which must also be considered. All of these effects influence the initial and final density scale length. They provide an explanation for both the measured maximum ion energy and the bremsstrahlung scaling with intensity that is so indicative of resonance absorption. Higher contrast ratio pulses have provided the signature for vacuum heating[23] which Brunel first described as ''not so resonant-resonance absorption.''[8] Rippling of the critical density surface is also known to enhance resonance absorption. The effects of hole boring and magnetic field formation on the absorption processes will be the subject of further investigation, preferably at higher intensities when these effects will be much more pronounced.

In Gibbon's model, the ponderomotive pressure pushes onto the overdense plasma, causing a shock wave to travel into the target. This shock will cause the plasma temperature and pressure in the overdense region to rise and this effect may provide an explanation for the observed multiple temperature phenomena. Another possible explanation for this effect may be that while ~50% of the laser energy is contained within the focal spot, the rest is contained in the waste of the laser beam (which is ~140 μm diameter from Sec. III B). This area has a much lower intensity than the main focal region, but the heating produced may still be sufficient to register on the spatially integrated x-ray detectors.[21]

V. SUMMARY AND CONCLUSIONS

We have reported some of the first measurements of picosecond laser interaction with solid targets for intensities up to 10^{19} W cm^{-2}. We have shown that the maximum ion energy scales as $E_{\max}=1.2(\pm 0.3)\times 10^{-2}\,[I/(\mathrm{W\ cm^{-2}})]^{0.313\pm 0.03}$ keV. Measurements of K-alpha x-ray spectra and x-ray/γ-ray bremsstrahlung confirm the $T_{\mathrm{hot}}\sim(I\lambda^2)^{1/3}$ scaling. These measurements are consistent with a resonance absorption process when the laser intensity contrast ratio is $1{:}10^{-6}$.

ACKNOWLEDGEMENTS

The authors gratefully acknowledge the assistance of Dr C. B. Edwards for the use of the shear interferometer, and to discussions with Dr. C. Darrow of Lawrence Livermore National Laboratory and Dr. A. Djaoui of Rutherford Appleton Laboratory (RAL). This work could not have been carried out without the assistance of the laser operations, target preparation, engineering staff at the Central Laser Facility of RAL.

The work was supported by the United Kingdom Engineering and Physical Sciences Research Council.

[1] D. Strickland and G. Mourou, Opt. Commun. **56**, 219 (1985).
[2] S. C. Wilks, W. L. Kruer, M. Tabak, and A. B. Langdon, Phys. Rev. Lett. **69**, 1383 (1992).
[3] W. L. Kruer and S. C. Wilks, Plasma Phys. Controlled Fusion **34**, 2061 (1992); S. C. Wilks, Phys. Fluids B **5**, 2603 (1993).
[4] S. C. Wilks, W. L. Kruer, and W. B. Mori, IEEE Trans. Plasma Sci. **PS-21**, 120 (1993); S. V. Bulanov, N. M. Naumova, and F. Pegoraro, Phys. Plasmas **1**, 745 (1994); S. Kohlweyer, G. D. Tsakiris, C.-G. Wahlström, C. Tillman, and I. Mercer, Optics Commun. **117**, 431 (1995); D. Von de Linde, T. Engers, G. Jenke, P. Agostini, G. Grillon, E. Nibbering, A. Mysyrowitz, and A. Antonetti, Phys. Rev. A **52**, R25 (1995).
[5] P. Gibbon, Phys. Rev. Lett. **76**, 50 (1996); P. A. Norreys, M. Zepf, S. Moustaizis, A. P. Fews, J. Zhang, P. Lee, M. Bakarezos, C. N. Danson, A. Dyson, P. Gibbon, P. Loukakos, D. Neely, F. N. Walsh, J. S. Wark, and A. E. Dangor, Phys. Rev. Lett. **76**, 1832 (1996).
[6] M. Tabak, J. Hammer, M. E. Ginsky, W. L. Kruer, S. C. Wilks, and J. Woodworth, Phys. Plasmas **1**, 1626 (1994),
[7] D. W. Forslund, J. M. Kindel, K. Lee, E. L. Lindman, and R. L. Morse, Phys Rev A **11**, 670 (1975); G. J. Pert, Plasma Phys. **20**, 175 (1978), and references therein.
[8] F. Brunel, Phys. Rev. Lett. **59**, 52 (1987); Phys. Fluids **31**, 2714 (1988).
[9] P. Gibbon and A. R. Bell, Phys. Rev. Lett. **68**, 1535 (1992); P. Gibbon, Phys. Rev. Lett. **73**, 667 (1994); H. Ruhl and P. Mulser, Phys. Lett. A **205**, 388 (1995).
[10] A. A. Andreev, E. G. Gamaly, V. N. Novikov, A. N. Semaklin, and V. T. Tikhonchuk, Sov. Phys. JETP **74**, 963 (1994).
[11] D. F. Price, R. M. More, R. S. Walling, G. Guethlein, R. L. Shepherd, R. E. Stewart, and W. E. White, Phys. Rev. Lett. **75**, 252 (1995).
[12] B. N. Chichkov, Y. Kato, and M. Murakami, Phys Rev A **46**, 4512 (1992); J. Denavit, Phys. Rev. Lett. **69**, 3053 (1992).
[13] S. J. Gitomer, R. D. Jones, F. Begay, A. W. Ehler, J. F. Kephart, and R. Kristal, Phys. Fluids **29**, 2679 (1986).
[14] H. M. Milchberg, R. R. Freeman, S. C. Davey, and R. M. More, Phys. Rev. Lett. **61**, 2364 (1988); J. C. Kieffer, P. Audebert, M. Chaker, J. P. Matte, H. Pepin, T. W. Johnson, P. Maine, D. Meyerhofer, J. Delettrez, D. Strickland, P. Bado, and G. Mourou, *ibid*. **62**, 760 (1989); R. Fedosejevs, R. Ottmann, R. Sigel, G. Kuhnle, S. Szatmari, and F. P. Schafer, *ibid*. **64**, 1250 (1990).
[15] D. Klem, C. Darrow, S. Lane, and M. D. Perry, in *Short Pulse High Intensity Lasers and Applications II*, edited by H. A. Baldis, Proceedings of the International Society for Optical Engineering (International Society for Optical Engineering, Bellingham, WA, 1993), Vol. 1860, pp. 98–101.
[16] M. Schnurer, M. P. Kalashinokov, P. V. Nickles, Th. Schlegel, W. Sander, N. Demchenko, R. Nolte, and P. Ambrosi, Phys. Plasmas **2**, 3106 (1995).
[17] D. D. Meyerhofer, H. Chen, J. A. Delettrez, B. Soom, S. Uchida, and B. Yaakobi, Phys. Fluids B **5**, 2584 (1993).
[18] A. Rousse, P. Audebert, J. P. Geindre, F. Fallies, J. C. Gauthier, A. Mysyrowicz, G. Grillon, and A. Antonetti, Phys. Rev. E **50**, 2200 (1994).
[19] J. D. Kmetec, C. L. Gordon, J. J. Macklin, B. E. Lemoff, G. S. Brown, and S. E. Harris, Phys. Rev. Lett. **32**, 1420 (1992).
[20] Z. Jiang, J. C. Kieffer, J. P. Matte, M. Chaker, O. Peyrusse, D. Gilles, D. Korn, A. Maksimchuk, S. Coe, and G. Mourou, Phys. Plasmas **2**, 1702 (1995).
[21] U. Teubner, I. Ushmann, P. Gibbon, D. Altenbernd, E. Forster, T. Feurer, W. Theobold, R. Sauerbrey, G. Hirst, M. H. Key, J. Lister, and D. Neely, ''Absorption and hot electron production by high intensity UV laser pulses in solid targets,'' Phys. Rev. E (in press).
[22] P. Gibbon and E. Forster, Plasma Phys. Controlled Fusion **38**, 769 (1996).
[23] G. Malka and J. L. Miquel, Phys. Rev. Lett. **77**, 75 (1996).
[24] C. N. Danson, L. J. Barzanti, Z. Chang, A. E. Damerell, C. B. Edwards, S. Hancock, M. H. R. Hutchinson, M. H. Key, S. Luan, R. R. Mahadeo, I. P. Mercer, P. Norreys, D. A. Pepler, I. N. Ross, M. A. Smith, R. A. Smith, P. Taday, W. T. Toner, K. W. M. Wigmore, T. B. Winstone, R. W. W. Wyatt, and F. Zhou, Opt. Commun. **103**, 392 (1993).
[25] C. N. Danson, N. Bradwell, L. J. Barzanti, J. Collier, A. Damerell, C. B. Edwards, C. Johnson, M. H. Key, D. Neely, M. Nightingale, D. A. Pepler, I. N. Ross, P. Ryves, C. Stephens, N. Thompson, M. Trentelman, E. Wolfraum, F. N. Walsh, and R. Wyatt ''Characterisation of the VULCAN Nd: glass laser for multi-terawatt operation,'' in *Proceedings of the 24th European Conference on Laser Interaction with Matter (ECLIM)*, Madrid, Spain, 1996 (Institute of Physics, Bristol, in press).
[26] A. P. Fews, M. J. Lamb, and M. Savage, Opt. Commun. **94**, 259 (1992).
[27] J. Zhang, M. Zepf, P. A. Norreys, A. E. Dangor, M. Bakarezos, C. N. Danson, A. Dyson, A. P. Fews, P. Gibbon, M. H. Key, P. Lee, P. Loukakos, S. Moustaizis, D. Neely, F. N. Walsh, and J. S. Wark, Phys. Rev. A **54**, 1597 (1996).
[28] A. P. Fews and D. Henshaw, Nucl. Instrum. Methods Phys. Res. **197**, 512 (1982); A. P. Fews, Nucl. Instrum. Methods Phys. Res. Sec. B **72**, 91 (1992).
[29] D. M. Corallo, D. M. Creek, and G. M. Murray, J. Phys. E: Sci. Instrum. **13**, 623, (1980).
[30] J. D. Hares, J. D. Kilkenny, M. H. Key, and J. G. Lunney, Phys. Rev. Lett. **42**, 1216 (1979).

[31]G. D. Enright, M. C. Richardson, and N. H. Burnett, J. Appl. Phys. **50**, 3909 (1979).
[32]F. Amiranoff, E. Eidmann, R. Sigel, R. Fedosejevs, A. Maaswinkel, Y. L. Teng, J. D. Kilkenny, J. D. Hares, D. K. Bradley, B. J. MacGowan, and T. J. Goldsack, J. Phys. D **15**, 2463 (1982).
[33]N. A. Ebrahim, C. Joshi, and H. A. Baldis. Phys. Rev. A **25**, 2440 (1982).
[34]N. H. Burnett, G. D. Enright, A. Avery, A. Leon, and J. C. Kieffer, Phys. Rev. A **29**, 2294 (1984).
[35]B. Luther-Davies, A. Perry, and K. A. Nugent. Phys. Rev. A **35**, 4306 (1986).
[36]D. H. Lumb and A. D. Holland, Nucl. Instrum. Methods. Phys. Res. A **273**, 696 (1988).
[37]M. Green and V. Cosslett, Proc. R. Soc. London **78**, 1206 (1961).
[38]B. L. Henke, P. Lee, T. J. Tanaka, R. L. Shimabukuro, and B. K. Fujikawa, At. Nucl. Data Tables **27**, 1 (1982).
[39]M. O. Krause, J. Phys. Chem. Ref. Data **8**, 307 (1979).
[40]T. Yabe and M. Hasegawa, Phys. Rev. Lett. **57**, 2667 (1986).
[41]A. Pukhov and J. Meyer-ter-Vehn, Phys. Rev. Lett. **76**, 3975 (1996).
[42]A. R. Bell, F. N. Beg, Z. Chang, A. E. Dangor, C. N. Danson, C. B. Edwards, A. P. Fews, M. H. R. Hutchinson, S. Luan, P. Lee, P. A. Norreys, R. A. Smith, P. F. Taday, and F. Zhou, Phys. Rev. E. **48**, 2087 (1993).
[43]C. B. Edwards (private communication, 1994).
[44]A. P. Fews, P. A. Norreys, F. N. Beg, A. R. Bell, A. E. Dangor, C. N. Danson, P. Lee, and S. J. Rose, Phys. Rev. Lett. **73**, 1801 (1994).
[45]J. S. Pearlman and R. L. Morse, Phys. Rev. Lett. **40**, 1652 (1978).
[46]T. H. Tan, G. H. McCall, and A. H. Williams, Phys. Fluids **27**, 296 (1984).
[47]Y. Kishimoto, K. Mima, T. Watanabe, and K. Nishihar, Phys. Fluids **26**, 2308 (1983).
[48]D. T. Attwood, D. W. Sweeney, J. M. Auerbach, and P. H. Y. Lee, Phys. Rev. Lett. **40**, 184 (1978).
[49]G. Guethlein, M. E. Foord, and D. Price, Phys. Rev. Lett. **77**, 1056 (1996).